Materials Today Communications 34 (2023) 105016

Contents lists available at ScienceDirect

Materials Today Communications

journal homepage: www.elsevier.com/locate/mtcomm

Statistical characterization of segregation-driven inhomogeneities in metallic microstructures employing fast first-order variograms

Santiago Benito [a,*], Gero Egels [a], Alexander Hartmaier [b], Sebastian Weber [a]

[a] Ruhr-Universität Bochum, Chair of Materials Technology, 44780 Bochum, Germany
[b] Chair of Micromechanical and Macroscopic Modelling, ICAMS, Ruhr-University Bochum, 44780 Bochum, Germany

ARTICLE INFO

Keywords:
Microstructural characterization
Geostatistics
Statistical description
Stochastic modeling
Random fields
Spatial data

ABSTRACT

The microstructure is the centerpiece connecting thermodynamic, compositional, and kinetic stochasticity with macroscopic behavior. As such, its thorough description is of fundamental importance: Microscopical spatial composition fluctuations can critically undermine or improve material performance. Still, both traditional and modern, state-of-the-art statistical microstructural characterization methods overlook micro and mesosegregations. Instead, they generally focus on microconstituent and grain examination. Segregation effects are thus commonly described on a case-by-case basis or employing parameters that lack spatial interpretation. We propose fast first-order variograms as a convenient statistical tool to comprehensively describe chemical segregations in metallic materials. First-order variograms are physically meaningful descriptors capable of revealing spatial variations and correlations. In particular, we discuss the derivation, application, advantages, and limits of their fast computation using the fast Fourier transform, which brings a substantial speed increase over the method-of-moments estimation. Furthermore, we compare them to popular texture characterization techniques borrowed from image processing and analysis. With this work, we establish a simple-to-use, yet powerful method to characterize the severeness of micro and mesosegregations and, thus, to quantify their influence on material behavior.

1. Introduction

All technological metallic materials exhibit segregations in the micro and mesoscales. They are nothing other than metastable spatial composition variations observable in a solid alloy, stemming from the solute solubility differences across phases. As materials solidify, the solid (either dendritic or cellular) regions push away or pull into them solute atoms. The composition fluctuations produce, in turn, spatial changes in the material properties. Far from inconsequential, these can lead to material failure or a substantial increase in mechanical properties. Here are some examples:

- In cobalt and nickel-based single-crystal superalloys, solute homogenization is critical, as it ensures consistent creep resistance [1,2].
- Chemical inhomogeneities in austenitic stainless steels deployed in hydrogen-rich environments undermine their resistance against hydrogen embrittlement, as they compromise the stability of the austenite phase [3].
- The metastable cellular segregation/dislocation structure observed in many additively manufactured specimens hinders dislocation movement, thus increasing their strength [4,5].
- The composition difference between dendrites and interdendritic spaces in high-entropy alloys affects the precipitation of intermetallic compounds, and effectively governs the emerging micromechanical properties [6,7].
- The powder solidification structure influences the carbide size and morphology in HIP'ed high-alloyed tool steels [8].

Applying electron microscopy, we can describe the resulting segregations in the solid alloys through electron probe microanalysis (EPMA) and energy-dispersive X-ray spectroscopy (EDS) [1,3,5–7,9–11]. These chemical characterization techniques can provide elemental mappings – sometimes called composition fields –, i.e., two-dimensional matrices whose elements quantify the chemical composition of that small portion of the material. These mappings are essentially digital images. The sole (and fundamental) difference is that the matrix elements in these mappings are real-valued and not discrete intensity levels as in image pixels. Usually, elemental mappings are accompanied by secondary electron (SE) or backscatter electron (BSE) detector micrographs that provide context to the measurements. Additional electron backscatter diffraction (EBSD) measurements can provide crystallographic information in the sampled area [1,3,5–7,9,10].

* Corresponding author.
E-mail address: santiago.benito@rub.de (S. Benito).

https://doi.org/10.1016/j.mtcomm.2022.105016
Received 5 June 2022; Received in revised form 8 November 2022; Accepted 22 November 2022
Available online 24 November 2022

The quantitative evaluation of chemical homogeneity usually involves a case-by-case comparison of selected parameters. Arguably, the most popular approach is the computation of partition coefficients k [1]. The use of the partition coefficient in metallic materials is tightly related to the Scheil–Gulliver equation [12]:

$$c_s = kc_0(1 - f_s)^{k-1},$$

where c_s and c_0 are the element concentrations in weight percent in the solid and the alloy, respectively. f_s, on the other hand, is the solid fraction. To obtain k for a given element, one sorts all concentrations c_s in the corresponding mapping according to f_s and fits the Scheil–Gulliver equation. The sorting operation thus requires the selection of a reference element. Koßmann et al. for instance, chose cobalt because is the basis element of the studied alloy [1]. While the partition coefficient has a sound physical basis, it also has drawbacks. Namely, it does not convey geometric or spatial information and is not suitable for describing other types of segregation, such as grain boundary segregations. Moreover, it requires knowledge of the solidification process, which is not always fully understood. This complication applies, for instance, to metastable cellular microstructures [13]. Finally, it cannot directly describe the homogeneity of properties emerging from segregations like austenite stability.

Other, perhaps simpler, approaches include the global maximum to minimum ratio and the computation of the standard deviation across a series of scan lines or in a complete map [10,14,15]. Another alternative is employing texture description methods from signal and image processing and analysis. These are, however, normalized such that they return values within given ranges and thus lack direct physical interpretation. The most common examples are the properties derived from the gray-level co-occurrence matrix (GLCM): contrast, correlation, energy, and homogeneity, which have found application in microstructural characterization [16,17]. For example, the homogeneity parameter has a valid span between zero and unity; unity values correspond to a constant value throughout the map, while lower values indicate increasing degrees of heterogeneity. Moran's I autocorrelation measure is more thorough but is also normalized [18]. Another potential shortcoming is that these image-based approaches can take comparatively long times to produce a result.

Classic and modern microstructural characterization methods essentially deal with *random heterogeneous materials*. These have more than one microconstituent or, if they are single-phase, present polycrystalline texture [19]. The word *random* indicates that the microstructure is intrinsically the result of a stochastical process [20]. Thus, they best describe, for example, precipitates, inclusions, and grain structures [21–23]. The method proposed in this work targets spatial chemical variations and derived properties in single-phase materials or within a single constituent. Hence, in the jargon of stochastic physics, it characterizes inhomogeneities and the resulting local properties in random *homogeneous* materials.

The field of statistics dealing with the quantitative description of variables distributed in space (and time and space) is called *geostatistics* [24]. Matheron coined the term geostatistics in 1962, specifically for ore reserve evaluation. Since then, and through constant development as a multi-disciplinary field, it has appealed to a greater audience. Nonetheless, research works employing methods borrowed from this branch of statistics are rare in materials science and virtually nonexistent in engineering materials characterization and development. That said, within materials discovery and combinatorial science, these techniques do enjoy popularity because of their interpolation and predictive power. The most relevant descriptive tool in geostatistics is the *variogram*, which describes how the values of a given property at two points in a field change as the distance between them varies. Variograms come in different flavors, the most widespread being the variograms of orders two and one. Of the two, the order-two version is generally several orders of magnitude faster to compute, thanks to the method-of-moments estimation through the convolution theorem and the fast Fourier transform [25]. Yet, the first-order variogram has a more straightforward physical interpretation that renders it better suited for analyzing segregation-driven inhomogeneities.

In this paper, we show how to employ knowledge of the marginal distribution of elemental and property mappings to compute fast first-order variograms. Our goal is to demonstrate a fast and reliable method that delivers a targeted quantification grounded on physical meaning. We examine the estimator derivation, the limits of the technique, and present both numerical and real application examples. Finally, we compare this approach to image-based texture description methods and outline its application for microstructural reconstruction.

This work was entirely written as a MATLAB® live script, which the reader can download from the complementary files section. Its interactive nature facilitates the adaption of these methods to other undertakings.

2. Fast (geo)statistical description

The stochastical nature of metastable thermodynamic states implies that slightly different properties will emerge in specimens processed identically. This statement holds macroscopically, but it also does at the micro-level—even if we could perform measurements at the same position with arbitrary precision. The intrinsic randomness of phase nucleation, growth, and coarsening motivates the introduction of stochastic models to uncover and understand the process-structure links that dominate modern materials science and technology [20]. In this context, we can define $Z(s,t)$, the local concentration of an arbitrary element at position s, and time t, as a random – or stochastic – quantity. As previously mentioned, each specimen will present a distinct version of $Z(s,t)$. In geostatistics, this is called a realization of the random field, which we denote as $Z(s,t;\omega)$. The combination of the concentrations of the n alloying elements $Z^i(s,t;\omega)$, with $i = 1, 2, \ldots, n$ and the nature of the solidification process itself create the material microstructure, which is also a random field. Formally, the microstructure is generally called a structure-function $\xi(s,t)$ with realizations $\xi(s,t;\omega)$ [26]. The structure-function is a general construct that changes according to the material and application studied. For instance, in multiphase materials, $\xi(\cdot)$ describes the disjoint regions that define the phase domains. In the case of this work – and drawing from the examples in the introduction – $\xi(\cdot)$ might describe local austenite stability, dislocation density, or microhardness. We will not consider time as a variable in the following derivation. However, it is useful to commit to memory that for in-situ heat treatment modeling, t is an important variable.

As mentioned in the introduction, variograms are the leading description tool in the geostatistics toolbox. Variograms are closely related to the two-point probability functions (also known as two-point statistics) and two-point correlation functions [27] used since the end of the last century to characterize [26,28] and reconstruct [19,29] random heterogeneous microstructures. The variogram is defined as:

$$2\gamma\left(s_1 - s_2\right) = \mathrm{var}\left(\xi(s_1) - \xi(s_2)\right), \tag{1}$$

where $s \in \mathbb{R}^d$ and s_1 and s_2 are the positions at which we observe the property $\xi(\cdot)$, and $\mathrm{var}(\cdot)$ is the variance. Intuition (and a basic understanding of the diffusion behavior of interstitial and substitutional alloying elements and solidification sequences) suggests that two close points will show similar property values. Conversely, at greater distances, where the solidification and chemical conditions are different, we expect greater variations. By quantifying the spatial difference, variograms reveal correlation patterns. A constant, nonzero variogram indicates that the inhomogeneities are uncorrelated. This is, for instance, the case in uniformly distributed random noise, also known as static noise. If the variogram presents repeating, wave-like shapes, a strong spatial correlation exists in the microstructure. Only a constantly zero-valued variogram corresponds to a perfect homogeneity.

If the underlying stochastic process is intrinsically stationary, i.e., the mean value of a sufficiently large map at the positions s_1 and

s_2 is the same, we can directly compute the variogram using the method-of-moments (MoM) estimator:

$$2\gamma(h) = \frac{1}{N(h)} \sum_{N(h)} \left(\xi(s_1) - \xi(s_2)\right)^2, \tag{2}$$

with $h = s_1 - s_2$, $h \in \mathbb{R}^d$. $N(h)$ is the number of distinct data pairs separated by h. To put it in words, the variogram is the mean squared difference of the random field values at positions separated by a distance h. For more information on valid variograms see the works by Cressie and Chilès [24,27]. We have purposefully refrained from introducing further definitions and validity conditions – such as conditional negative-definiteness – to keep this section concise.

In EPMA and EDS mappings and, by extension, property mappings, the stationarity condition generally guaranteed as a consequence of dendrite scale in relation to the macroscopic geometry and the imaging method. We deal with two-dimensional data arranged in a grid analogous to the pixels we find in images. This simple fact allows us to rewrite Eq. (2) using simple operations from signal and image processing to speed up the estimation:

$$2\gamma(h) = \frac{f^2 \star I_f + I_f \star f^2 - 2(f \star f)}{I_f \star I_f}, \tag{3}$$

where $s, h \in \mathbb{R}^2$, $\star$ is the cross-correlation operator, the exponent indicates element-wise power, f is a matrix containing a grid sampling of the realization $\xi(\cdot;\omega)$, and I_f is an index matrix containing ones in the positions where there is a valid data element in f. The cross-correlation is a mathematical operation from signal and image processing that describes the similarity between the operands. By removing[1] a data point in f and, correspondingly, assigning a zero in its I_f counterpart, the estimator effectively excludes the position from the analysis. Here, we use this control to limit the analysis area to the phase of interest in multi-phase or composite materials. The speed increase linked to this last mathematical representation comes from the convolution theorem. Marcotte showed how to use the fast Fourier transform (FFT) to perform variogram computations in a fraction of the time required by the standard estimator in Eq. (2) [25,30]. Since $h \in \mathbb{R}^2$, the variogram $2\gamma(h)$ is also a matrix and is sometimes called a variogram map. Similar to two-point probability functions, these maps are point symmetric with respect to their center: to find the mean squared difference between all points separated by a Euclidean vector of a given magnitude and direction, one has to place that same vector at the center and read the result in the resulting element. Thus, a radial average reduces the dimensionality of the descriptor because it returns the mean across all directions. For microstructures showing anisotropy along a certain axis, we can derive one-dimensional parameters in the desired orientation. The fundamental difference between two-point probability functions and variograms lies in their output. The former return the probability of finding the same phase at the end of a vector of given length and orientation. On the contrary, the latter describe the difference in the property value at the point pairs separated by said vector.

Given that it computes the expected value of squared differences, we call $2\gamma(h)$ a variogram of order two. Variograms of order one, sometimes called *madograms*, employ the absolute difference:

$$2\gamma_1(h) = \frac{1}{N(h)} \sum_{N(h)} |\xi(s_1) - \xi(s_2)| \tag{4}$$

First-order variograms are more interesting for the case study of this work than their second-order counterparts:

- Segregations and related structure fluctuations are best expressed in the same units as the originally measured property.
- The square operation in second-order variograms gives more weight to larger differences.
- Dividing the first-order variogram by the mean property value produces a bounded, unitless measure of the inhomogeneity.

Nevertheless, due to the impossibility of writing the absolute value operation in terms of cross-correlations or convolutions, computing first-order variograms directly is not a fast task. However, with some previous knowledge of the marginal distribution of the property values, we can derive first-order variograms from regular variograms [24]. In fact:

$$2\gamma_1(h) = \begin{cases} \sqrt{\dfrac{\gamma(h)}{\mathrm{var}\,(\xi)}}\,\mathrm{MD}(\xi)\ , \text{ if cond. (I) holds;} & \text{(a)} \\ \gamma(h)\dfrac{\mathrm{MD}\,(\xi)}{\mathrm{var}\,(\xi)}, \text{ if cond. (II) or (III) holds,} & \text{(b)} \end{cases} \tag{5}$$

where the conditions are: (I) $\left(\xi(s_1) - \xi(s_2)\right)$ is normally distributed, (II) $\xi(\cdot)$ is uniformly distributed, and (III) independent identically distributed random values are assigned to cells of a random partition. $\mathrm{MD}(\cdot)$ is an estimator of the absolute mean difference [24]. In general, the linear combination of two correlated normally distributed random variables produces a still normally distributed random variable. This means that if the marginal distributions $\xi(\cdot)$ are normally distributed, we can assume $\left(\xi(s_1) - \xi(s_2)\right)$ is normally distributed, too. As we will illustrate in the following section, the segregation patterns observed in metallic materials – and the thus induced property fluctuations – can be associated with one of the three cases presented in Eq. (5).

Three variogram features generally stand out: The range, the sill, and the nugget effect. If the variogram values stabilize around a value as $|h| \to \infty$, then the sill is that value. The range, on the other hand, is the smallest value $|h_0|$ such that $2\gamma\left(h_0(1+\varepsilon)\right)$ is the sill for any $\varepsilon > 0$. In simpler terms: at Euclidean distances larger than the range, there is no correlation between two points in the map. Nonetheless, these parameters may not exist for all random fields or even all directions in the variogram maps. Finally, the nugget effect is a discontinuity near the origin, i.e., the variogram tends to a value other than zero when $h \to 0$. As a consequence of their discrete spatial nature, all variograms computed from elemental mappings will exhibit this *jump* near the origin. The magnitude of the nugget effect is therefore tied to the spatial resolution. In the context of segregation analysis, order statistics are also worth highlighting. These are the minimum, maximum, and median variogram values and the first and third quartiles. They enable, together with the mean value, straightforward specimen comparisons in terms of scalar descriptors. These measures can be applied to all variograms, independently of their order and direction.

As implied in the previous paragraphs, variograms can be isotropic and anisotropic. In the former case, a variogram of any order is solely a function of $|h|$. Anisotropic property maps and microstructures present variograms that vary additionally with orientation. For instance, different directions might have the same sill but distinct ranges. Alternatively, one direction can exhibit an unbounded variogram while a perpendicular one attains a sill.

In intrinsically stationary stochastic processes, dividing the variogram of order one by two times the mean map value μ produces a unitless measure of the homogeneity, the Gini coefficient variogram:

$$\gamma_G(h) = \frac{\gamma_1(h)}{\mu} \tag{6}$$

$\gamma_G(h)$ can take values in the interval $[0, 1)$ and is a spatial extension of the Gini coefficient in econometrics [24,31]. $\gamma_G(h) = 0$ if the structure is homogeneous at the distance h. Oppositely, $\gamma_G(h) \to 1$ if the segregation state results in perfect inhomogeneity.

3. Application examples

In the following, we demonstrate the application of first-order variograms and their various derived measures. The three synthetic microstructures mainly validate the conditions (I)–(III) in Eq. (5) while

[1] Here, *removing* an element means setting to a special *undefined* data type: `NaN`, standing for Not a Number.

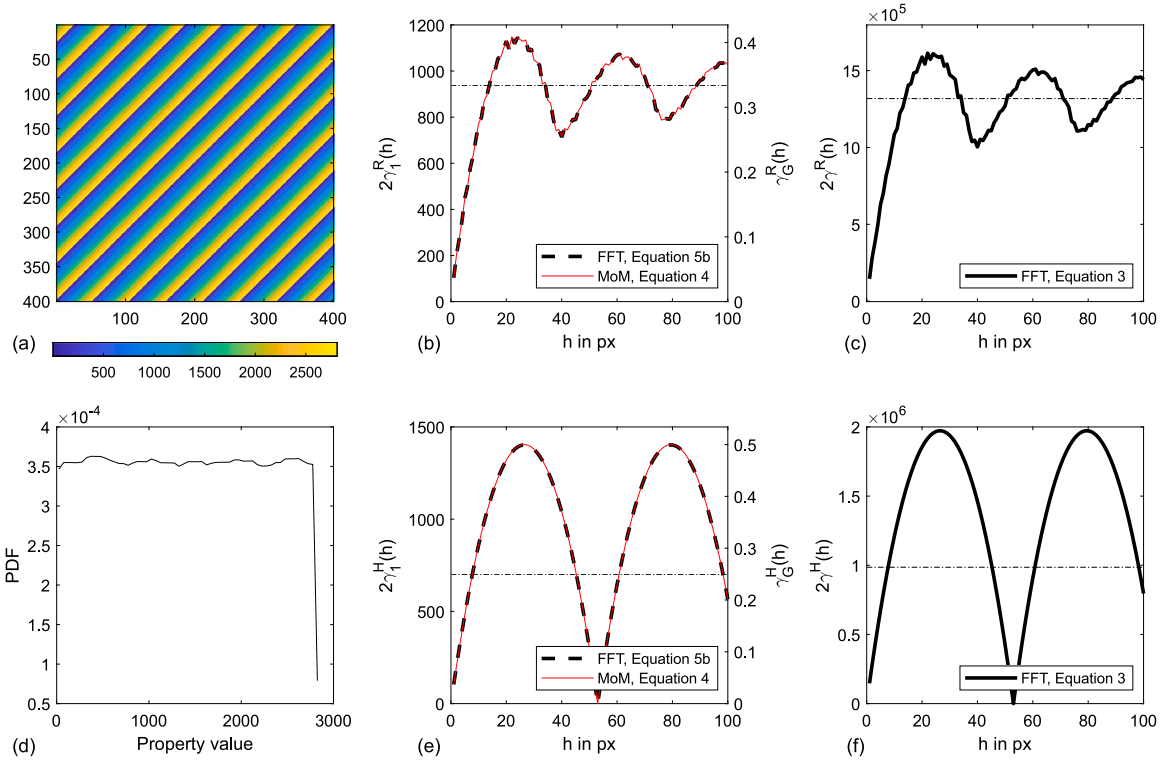

Fig. 1. Artificial microstructure with marginal uniform distribution and computed variograms. (a) Arbitrary mapping of the artificial microstructure. (b) Histogram of the data. (c) Radially averaged variogram of order one. (d) Radially averaged variogram of order two.

delivering some intuition for interpretation on their application in single-phase, chemically inhomogeneous materials. The homogeneity assessment on the austenitic steel 304L illustrates a real-world use case. It highlights graphical representation, parameter derivation, and analysis. We will not focus in this work on the use-case *statistical reconstruction*. We will, however, discuss the application in the summary and conclusions section.

3.1. Application on synthetic microstructures

The first example is a segregation structure with uniform marginal distribution and a diagonal repeating pattern of peaks and troughs similar to the high-ordered lamellar ultra-fine microstructure of eutectic high-entropy alloys [32]. We created it by feeding the MATLAB® `magic` function a prime number and repeating the result to form a bigger $n \times n$ matrix. The microstructure is displayed along with its histogram in Fig. 1(a) and (d), respectively. The property values are arbitrary; only their distribution is of interest in this analysis. Fig. 1(b) and (c) present the radially averaged variograms of orders one and two. In (b), the right y-axes corresponds to the radial average of the Gini coefficient variogram. The superscript R in the y-axis label indicates this radial examination. As a reminder: In (b), the variogram value is the expected absolute difference of two points separated by a distance h regardless of the orientation. In (c), instead of the absolute operation, the squared difference is employed. In Fig. 1(e) and (f), on the other hand, we present the horizontal variograms of order one and two, respectively. The strong contrast between these and the radial representations is a consequence of the microstructural anisotropy. Note that, because of the rotational symmetry along the axis perpendicular to the synthetic microstructure shown in Fig. 1(a), the horizontal and vertical orientations of the variogram are equivalent.

The variogram of order two was computed using the FFT because of the equivalence of Eqs. (2) and (3). The variogram of order one shows perfect agreement between the estimations using Eqs. (4) and (5)(b) even though the fast Fourier version is one around one thousand times faster than the MoM: 170 s and 0.17 s, respectively, employing a standard workstation with a 3.60 GHz AMD Ryzen 3 chip and 16 GB of RAM. We could reduce the computation time for Eq. (4) using parallelization to 100 s. For more insights on how the complexity of these operations impacts computation time, we refer the reader to the original work by Marcotte [25].

The periodic nature of the microstructure is evidenced in the variograms, which oscillate around the sill values. The sills are different in the radial and horizontal averages—this is another result of the observed anisotropy. Since we set 53 px as the original tile size in the `magic` function, we expect the horizontal period to be exactly 53 px, whereas in the radially averaged variogram it is $\sqrt{2\,(53\text{ px})^2/2} \approx 37.5$ px. The oscillations are reflective of the strong spatial correlation. As the distance between pairs of points increases, the oscillations dampen in the radial variograms as the result of the rise in number and variance of the values of the point pairs. For $h \to \infty$, i.e., at the macroscopic level, the radially averaged variogram will tend to its sill. Contrarily, the dampening effect does not appear along the horizontal and vertical axes because the original tiles are repeated precisely along those axes.

As presented in the previous section, we can derive additional homogeneity measures from the first-order variogram. For instance, the mean absolute difference is 905.55, which corresponds to a Gini coefficient of 0.322. Further, the maximum absolute difference we can expect between any two points in the field is 1146. The wealth of possible scalar descriptors together with the directionality selection make the variogram a versatile tool. In the remaining examples, we will illustrate other prospective measures.

We created the following segregation structure using the Kolmogorov–Petrovsky–Piskunov reaction–diffusion equation. Yang published a compact MATLAB® implementation of its finite differences solution [33]. The patterns that arise from the solution of these equations are called Turing's patterns. In Fig. 2(a) we present the microstructure, and in (b) we display its histogram. For instance, we can imagine that such a pseudo-random property map represents microsegregations at

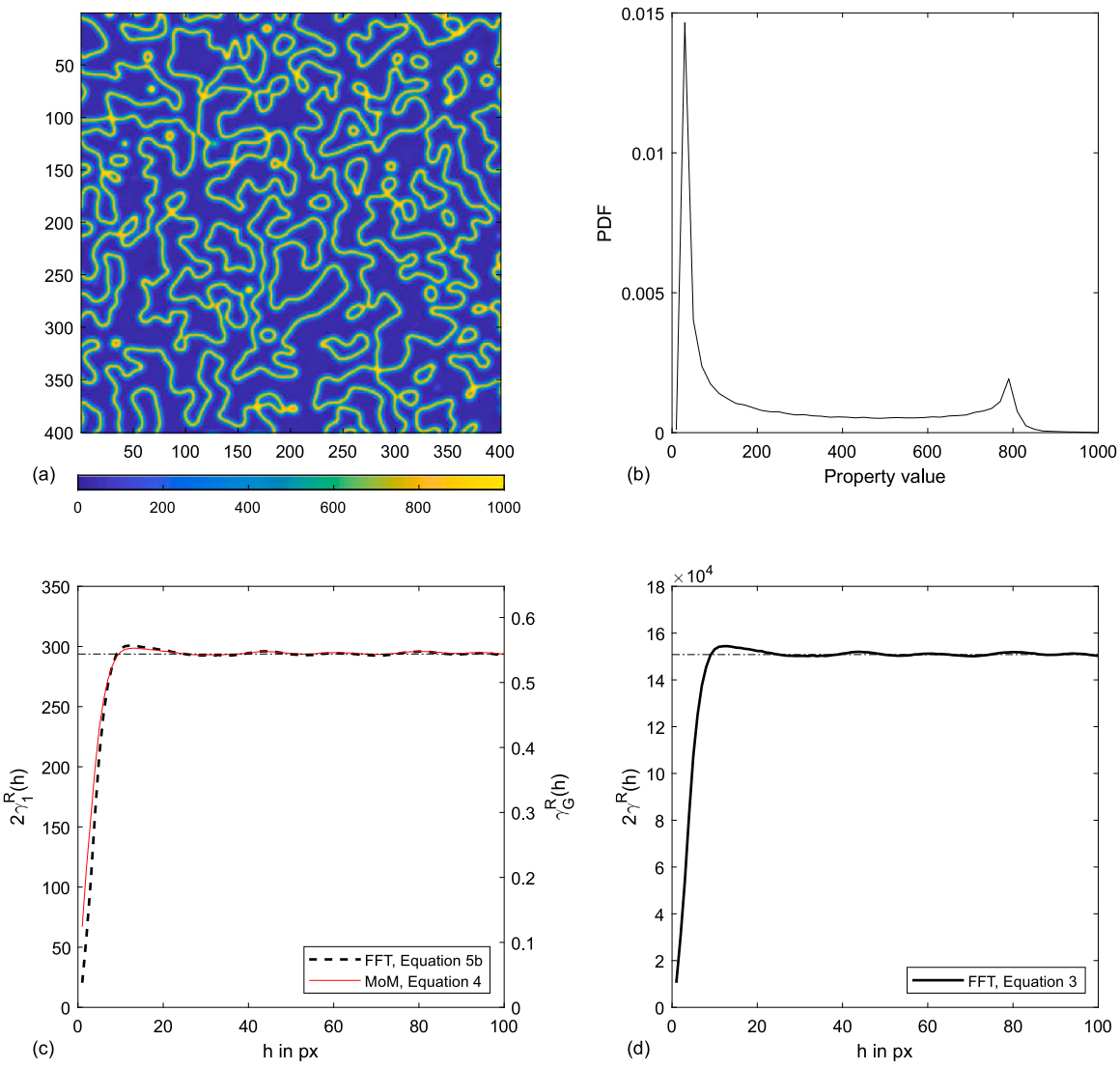

Fig. 2. Artificial microstructure with identically distributed random values in two random regions and computed variograms. (a) Arbitrary mapping of the artificial microstructure. (b) Histogram of the data. (c) Radially averaged variogram of order one. (d) Radially averaged variogram of order two.

the interfaces of an alloy consisting of at least two elements. Analogous to Fig. 1, we see in the bottom row the variograms of orders one and two.

From the histogram, we infer that the marginal distribution can be reasonably approximated to be composed of identically distributed random variables assigned to either region: Matrix or boundary. Thus, we compute the fast Fourier first-order variogram again using Eq. (5)(b). The agreement between the FFT approximation and the estimation is slightly off for small h values. The reason for this is that the diffusion equation does not create two sharply divided regions, and therefore there is a gradient in the represented property. The range in the radially averaged variograms is approximately 12 pixels, which corresponds to the segregation thickness in the regions we dubbed interfaces. The *bumps* around the sill with periodicity roughly equal to the mean free path in the matrix are the result of this correlation.

We modified the microstructure presented in Fig. 2 to create a normal marginal distribution, purposely adding Gaussian noise in the process. The resulting property map and histogram are in Fig. 3(a) and (b), respectively. We computed the first-order variogram in (c), correspondingly, using Eqs. (4) and (5)(a). The agreement in this instance is, again, excellent, with the FFT variant being around one thousand times faster. Lastly, we present the corresponding radially averaged variogram of order two in (d).

The new microstructure shows less spatial correlation than the original one, evidenced by its reduced matrix-boundary contrast. This correlation decrease manifests itself clearly in the variograms, which have no oscillations. Instead, the variograms monotonically increase to the sill. Since the spatial geometry in these last two property maps is identical, we observe the same range. The Gini variogram, on the other hand, presents lower values in Fig. 3, even though the variogram sills in Figs. 2(c) and 3(c) are comparable. This higher homogeneity is attributed to the mean value of the normally distributed mapping. In other words, their variability is similar in absolute terms, but relative to the mean value, the field in Fig. 3 is more homogeneous than its counterpart in Fig. 2.

3.2. Application example on the stainless austenitic steel AISI 304L

Austenitic stainless steels from the compositional range of AISI 316L exhibit a high resistance against hydrogen environment embrittlement (HEE) in a wide range of testing conditions [34,35]. This is related to their high austenite stability, i.e., the stability of the γ-austenitic face-centered cubic (fcc) lattice against a transformation to body-centered cubic (bcc) α'-martensite [36]. The $\gamma \rightarrow \alpha'$ transformation can either be thermally activated by cooling below the martensite start temperature (M_s), or induced by applying a mechanical load at temperatures

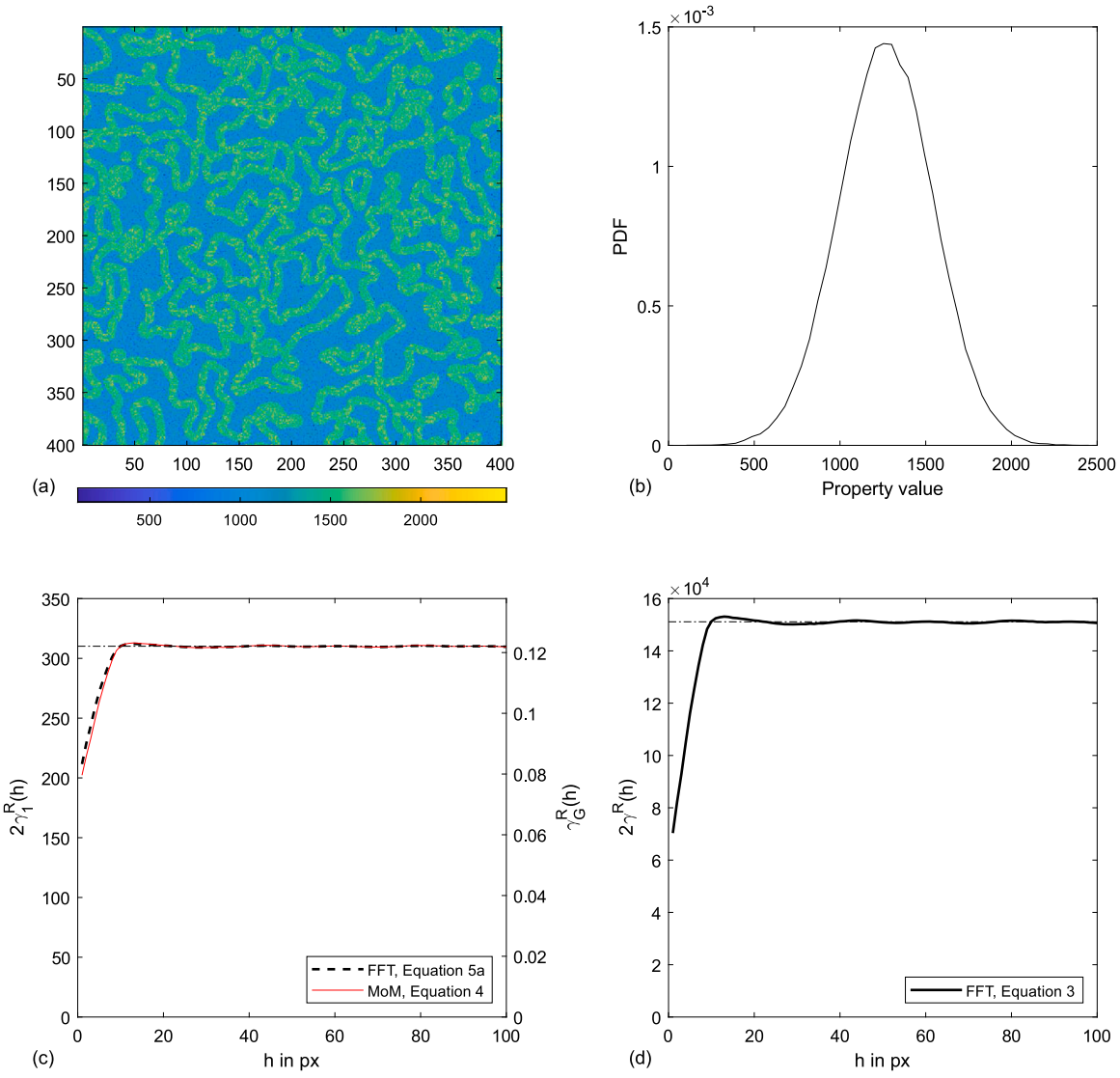

Fig. 3. Artificial microstructure with marginal normal distribution and computed variograms. (a) Arbitrary mapping of the artificial microstructure. (b) Histogram of the data. (c) Radially averaged variogram of order one. (d) Radially averaged variogram of order two.

below the M_d-temperature [37,38]. Once α'-martensite is present in an austenitic stainless steel, it deteriorates its resistance against HEE. That is because α'-martensite is inherently more susceptible to hydrogen-induced fracture than austenite and the diffusion of hydrogen atoms is multiple orders of magnitude faster in the bcc lattice than in the fcc lattice [36,39–41]. The austenite stability is therefore an important indicator for the resistance against HEE. Recent studies have shown that not only the global austenite stability, which is estimated based on the global alloy composition, influences the resistance against HEE, but also local variations of the austenite stability on the micro scale can have an impact [14,42]. Regions in the microstructure with locally reduced austenite stability provide favorable sites for α'-martensite formation and thereby facilitate hydrogen-induced crack formation and growth. Local variations of the austenite stability stem from element segregations that arise during the solidification in the steel casting process and remain throughout processing steps like forging and solution annealing [43,44]. Therefore, bars and flat products made of austenitic stainless steel typically exhibit band-like structures of high and low-alloyed regions in the microstructure [15].

Using the chemical composition from EDS mappings, we can compute the local thermodynamic driving force for the $\gamma \rightarrow \alpha'$ transformation $\Delta G^{\gamma \rightarrow \alpha'}$, and compute empirical descriptors such as M_s and M_d temperatures. For instance, the M_{d30} temperature, proposed by Nohara et al. [45], computes the temperature at which a true plastic strain of 30% causes a transformation of 50% of the austenite into α'-martensite.

For this case study, the material employed is the austenitic stainless steel AISI 304L (X2CrNi18-9, 1.4307). We show the results of four specimens that represent four usual conditions: (i) cast & rolled; cast, rolled and diffusion annealed at 1050 °C with two distinct durations, (ii) 5 h and (iii) 15 h; and, finally, (iv) electro-slag remelted (ESR) & rolled. The material used for conditions (i)–(iii) was produced in an industrial continuous casting process with a cross-section of 265 mm, and was subsequently hot-rolled to a bar shape with a diameter of 30 mm. The specimens for investigation were taken from the center of the bar. For condition (iv), the cast material was subjected to an industrial ESR process, in which an ingot with a diameter of 160 mm was produced. The ingot was then hot forged to a diameter of 50 mm. The chemical composition, as measured with optical emission spectrometry (OES), is given in Table 1.

We expect the austenite stability descriptor mappings to distinctly reveal the effects of the heat treatment and processing routes. For one, longer diffusion annealing times enable a more even distribution of the substitution elements that are ultimately decisive for local phase stability. The ESR step, on the other hand, reduces the range of macro

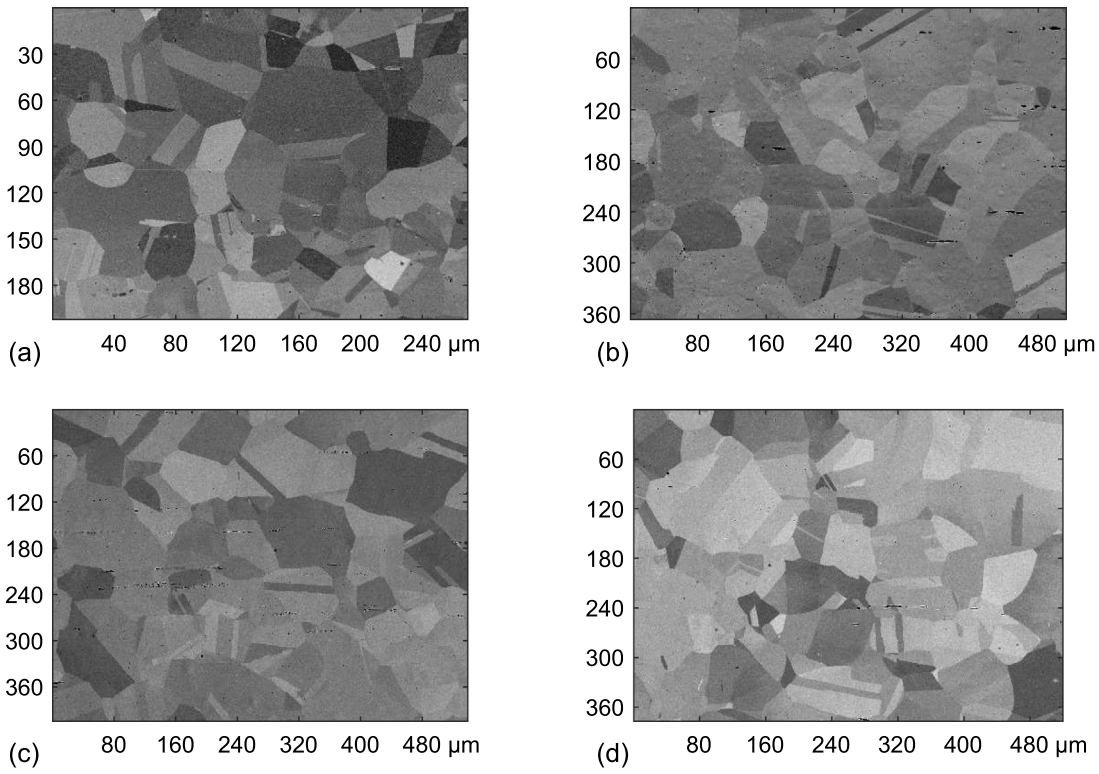

Fig. 4. BSE micrographs of the four AISI 304L (X2CrNi18-9, 1.4307) specimens. (a) Cast & rolled. (b) Cast, rolled, and annealed at 1050 °C for 5 h. (c) Cast, rolled, and annealed at 1050 °C for 15 h. (d) Electroslag remelted & rolled.

Table 1
Specimen chemical composition, measured with optical emission spectrometry in wt.%. The nominal composition is also provided as a reference. Note that in it, the values given for C, Si, and Mn are the max. bound.

Specimen	Fe	C	Si	Mn	Cr	Ni	N
X2CrNi18-9, nominal	Bal.	0.03	1.00	2.00	18.00	9.00	–
Cast and rolled & annealed	Bal.	0.02	0.68	1.97	17.98	8.48	0.06
ESR	Bal.	0.03	0.68	1.87	17.87	8.66	0.08

and micro segregations, thus producing a refined microstructure when compared with casting [46].

The descriptive power of variograms hinges on retrieving enough data to capture thoroughly the stochastic process at hand. Depending on the application, processing route, and specimen dimensions, it might be imperative to image several fields and present the corresponding statistics in the examination. Note that, for the purposes of this work, we limited ourselves to a relatively large area for each specimen. These can be seen in Fig. 4. Besides the expected austenitic grains we find MnS inclusions, visible as black horizontal lines and spots. These micrographs on their own do not provide any insight into the segregation-induced stability inhomogeneities.

Fig. 5 shows the driving force $\Delta G^{\gamma\to\alpha'}$ mappings of the four specimens, which we computed using the 2021a distribution of Thermo-Calc® and the database TCFE10 v10.1. Note that higher $\Delta G^{\gamma\to\alpha'}$ values indicate higher austenite stability. We recorded the EDS mappings of the elements Fe, Cr, Ni, Mn, Si, Mo, and Cu using an SEM TESCAN MIRA3 equipped with an Oxford Instruments EDS unit. The measurement fields were sampled such that the deformation direction coincides with the horizontal axis. The interface software AZtec®, also provided by Oxford Instruments, handled the data acquisition and evaluation. After binning, the size of each matrix element was 0.52 µm across all maps. We performed the complete data analysis in MATLAB®, using the academic version R2019b. We limited the processing to a 3 × 3 square median filtering, applied equally across all measurements. This step helps to bring back detail to the microsegregation structures as it reduces the Gaussian noise from the EDS measurements. There is no risk of information loss, as the maps are relatively large matrices. The variogram maps will evidence the spatial filtering performed: at distances smaller than the kernel size, the median filter will mask the true correlation of the data. We will be cognizant of this and remove those distances from the spatial analysis. We considered an even distribution of the elements C and N, with the corresponding concentration values given in the OES measurements. We set all MnS inclusions as `NaNs` to analyze exclusively the γ phase. In Fig. 5, we show these positions as white pixels.

In Fig. 5, the colormap scaling is the same for all mappings, meaning that a brief look already gives away qualitative information about them. In (a), the sample in the cast & rolled state clearly shows the above-mentioned band-like structures. These are less sharp in the annealed samples in Fig. 5(b) and (c); so much so that they are barely noticeable after fifteen hours of heat treatment. Finally, we see the same bands in the ESR sample, (d), albeit less distinct.

Leaving the qualitative observation to enter the quantitative analysis of the data, we start by presenting their normalized histograms in Fig. 6. Three pieces of information are immediately apparent: (i) the mean values are similar, (ii) the data is normally distributed in all cases, and (iii) the variance changes across samples.

Observation (i) is to be expected: All specimens have essentially the same global chemical composition. As for (ii), these mappings can be considered a linear combination of the local element concentrations [45], which, in turn, are generally also normally distributed. Even though the element distributions are not strictly independent or identically distributed, we consistently observed their weighted sum to converge to a Gaussian distribution. Finally, point (iii) reveals the first piece of information that leads to the interpretation of the variograms. The ESR sample shows the smallest variance, while the cast & rolled one has the largest. We expect to see these tendencies reflected in the sills of the variograms, provided they have one. However, as histograms

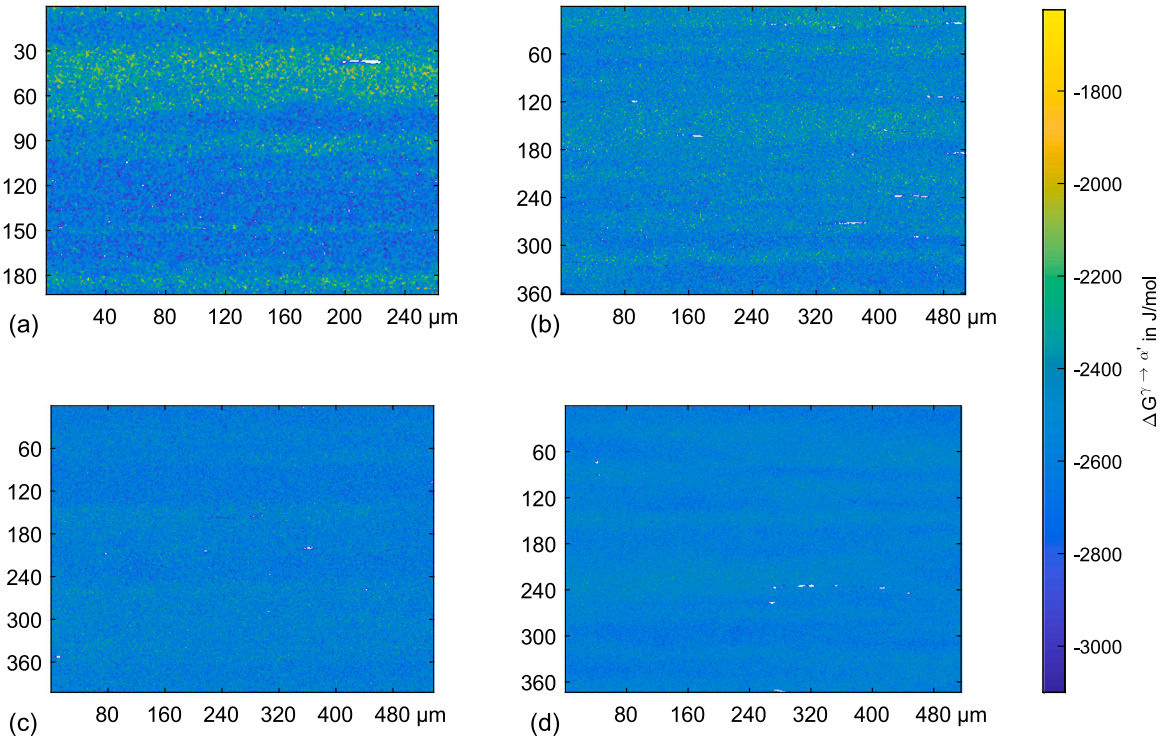

Fig. 5. Driving force $\Delta G^{\gamma\to\alpha'}$ mappings of the four AISI 304L (X2CrNi18-9, 1.4307) specimens. (a) Cast & rolled. (b) Cast, rolled, and annealed at 1050 °C for 5 h. (c) Cast, rolled, and annealed at 1050 °C for 15 h. (d) Electroslag remelted & rolled. (For interpretation of the references to color in this figure legend, the reader is referred to the web version of this article.)

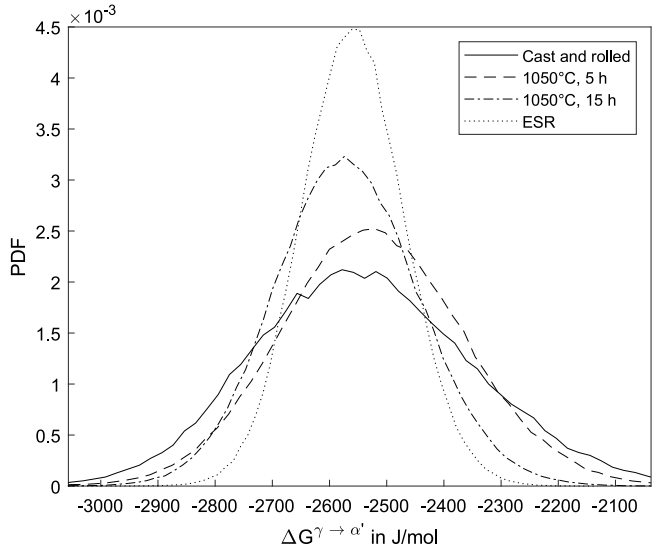

Fig. 6. Histograms of the driving force $\Delta G^{\gamma\to\alpha'}$ mappings of the four specimens.

do not provide spatial information, we cannot make statements about the area of influence or periodicity of the segregations.

The first-order variograms of all four specimens are laid out in Fig. 7. As we computed them for all directions, these are two-dimensional maps. We present $300\,\mu m \times 300\,\mu m$ fields to detail the changes in $\Delta G^{\gamma\to\alpha'}$ for distances up to $150\,\mu m$. We discarded the data points corresponding to distances shorter than 3 px $\approx 1.58\,\mu m$ to account for the median filtering. The boxplots next to the color bar indicate the quartiles of each variogram. The FFT computation time needed for each mapping in the workstation mentioned in the previous subsection was around 3 s. Contrarily, due to the size of the mappings, the MoM estimation required more than 130 s.

Contrary to the $\Delta G^{\gamma\to\alpha'}$ fields shown in Fig. 5, the corresponding $2\gamma_1$ maps look very dissimilar. For instance, by studying the box plot corresponding to the ESR specimen, we notice the maximum expected difference in $\Delta G^{\gamma\to\alpha'}$ between any two points is around 103 J/mol. In the cast & rolled sample, it is slightly above 240 J/mol. The specimen annealed for 15 h has the lowest variogram variance, indicating next to no correlation between points. The anisotropy appears as variations in the variograms in orthogonal directions. To get a tighter grasp on this effect, we computed the averaged first-order variograms we exhibit in Fig. 8; (a) presents a horizontally averaged version of the data, while, in (b), we show a vertically averaged account.

Let us begin by interpreting the horizontally averaged data. The first takeaway is that all variograms are virtually flat lines. The specimens essentially differ in their sill value. The cast & rolled sample exhibits the largest absolute differences, followed by the annealed samples. The ESR process cut the variogram values to roughly half of the original material. The vertical direction, which, again, is perpendicular to the deformation axis, offers more interesting insights. Here, the curves present oscillations and spatial variations associated with the deformation process. The five-hour-long annealing treatment effectively reduced the correlation intrinsic to the segregation bands. However, it did not manage to homogenize the material further. This behavior is evident in the relatively greater shift in the vertical variogram after the shorter annealing when compared to the horizontal one. The 15-h annealing produced a nearly isotropic structure: The vertical and horizontal variograms are flat lines revealing the same absolute differences regardless of distance. Still, despite its slight anisotropy, the ESR specimen has the best homogeneity. We can measure the range to $28\,\mu m$ in the five-hour annealed and ESR specimens. In the cast & rolled sample there is no apparent range, and the 15-h treated specimen, as explained above, shows no spatial correlation.

These observations can be complemented by targeted calculation of measures. Table 2 shows some parameters that quantify the isotropy

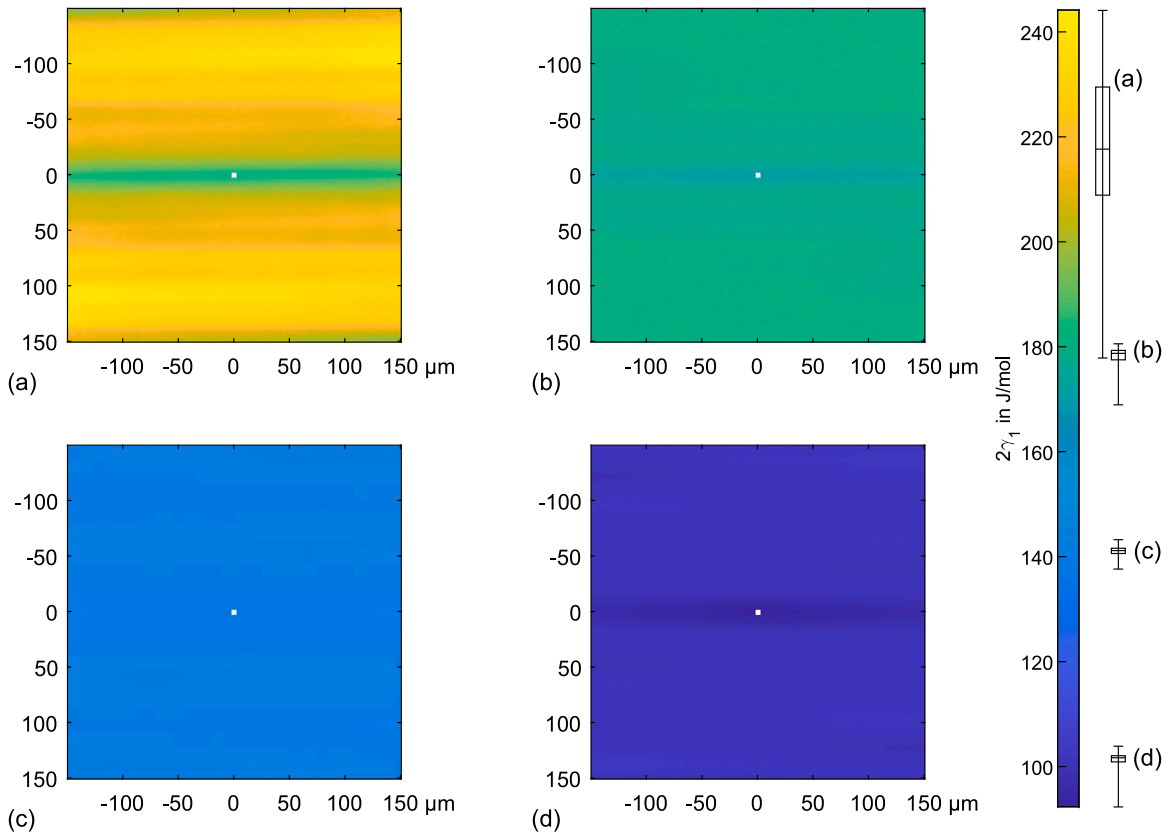

Fig. 7. Variograms of first order of the four samples in all directions. (a) Cast & rolled. (b) Cast, rolled, and annealed at 1050 °C for 5 h. (c) Cast, rolled, and annealed at 1050 °C for 15 h. (d) Electroslag remelted & rolled. The box plots show the variogram quartiles. (For interpretation of the references to color in this figure legend, the reader is referred to the web version of this article.)

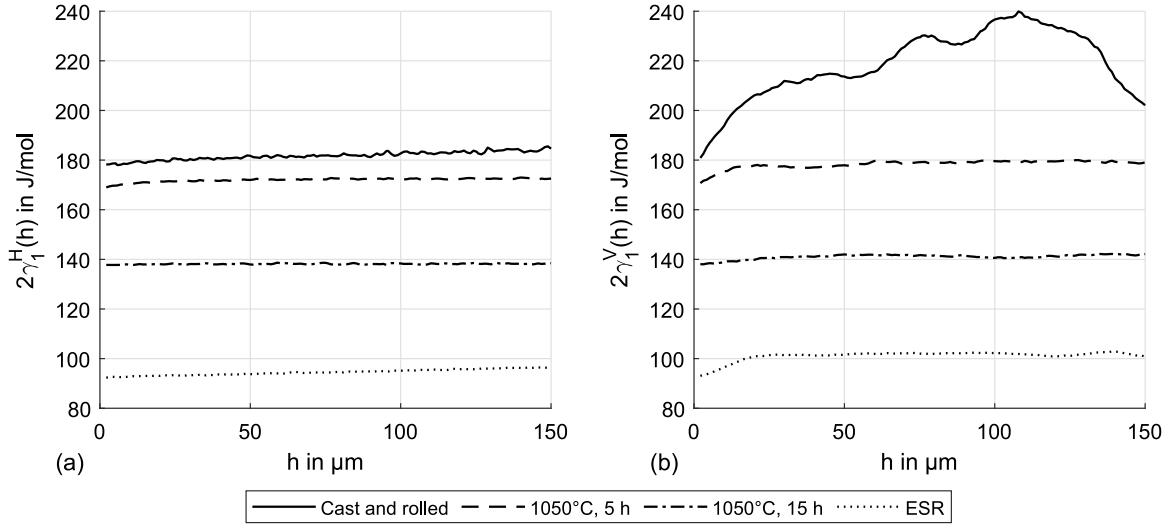

Fig. 8. Variograms of first order of the four samples. (a) Horizontal averages. (b) Vertical averages. The variograms of order one were derived from the fast computation of the variogram of order two using Eq. (5)(a).

and homogeneity of the specimens. For the vertical and horizontal directions, we present the minimum, maximum, and mean values of the first-order variograms and their Gini counterparts. Given the variogram shape, the minimum value coincides with the nugget effect. We further compare the annealed and ESR samples with the original material with the percentile relative difference measure Diff. = 100(1 − CR/PR). Here, CR stands for *cast & rolled* and PR for *processed*. The isotropy parameter is computed by dividing the mean variogram values in the deformation direction by its perpendicular analog. Increasing numbers indicate higher isotropy, with unity being the upper limit. In the bottom rows of Table 2, we present the minimum, maximum, and mean across all directions.

By tuning out the segregation band-line structures, the horizontal variogram provides information about the inhomogeneities solely caused by the solidification process. In its derived measures, we can assess the impact of the heat treatment on the general homogenization in

Table 2
Selected derived homogeneity measures for the horizontal and vertical directions. The relative difference shows the change with respect to the cast & rolled specimen. The isotropy measure results from dividing the mean horizontal and vertical variogram values. The global parameters in the bottom six rows are presented as reference.

			Cast & rolled	Annealed, 5 h		Annealed, 15 h		ESR	
				Val.	Diff.	Val.	Diff.	Val.	Diff.
Vertical	$2\gamma_1$ (J mol^{-1})	min	180.9	170.8	6 %	138.0	24 %	93.1	48 %
		max	240.0	180.0	25 %	142.2	41 %	102.9	57 %
		mean	219.1	178.4	19 %	141.1	36 %	101.2	54 %
	γ_G ($\times 10^{-2}$)	min	3.56	3.38	5 %	2.69	24 %	1.82	49 %
		max	4.73	3.57	25 %	2.77	41 %	2.01	58 %
		mean	4.32	3.53	18 %	2.75	36 %	1.98	54 %
Horizontal	$2\gamma_1$ (J mol^{-1})	min	178.0	169.0	5 %	137.7	23 %	92.4	48 %
		max	185.6	173.0	7 %	138.7	25 %	96.4	48 %
		mean	181.8	172.0	5 %	138.1	24 %	94.5	48 %
	γ_G ($\times 10^{-2}$)	min	3.51	3.35	5 %	2.68	24 %	1.80	49 %
		max	3.66	3.43	6 %	2.70	26 %	1.88	49 %
		mean	3.58	3.41	5 %	2.69	25 %	1.85	48 %
Isotropy		mean	0.839	0.964	16 %	0.979	18 %	0.934	13 %
Global	$2\gamma_1$ (J mol^{-1})	min	177.9	169.0	5 %	137.7	23 %	92.4	48 %
		max	244.2	180.6	26 %	143.3	41 %	103.9	57 %
		mean	218.2	178.3	18 %	141.0	35 %	101.1	54 %
	γ_G ($\times 10^{-2}$)	min	3.51	3.35	5 %	2.68	24 %	1.80	49 %
		max	4.81	3.58	26 %	2.79	42 %	2.03	58 %
		mean	4.30	3.53	18 %	2.75	35 %	1.98	54 %

the alloy. The vertical variogram, on the other hand, characterizes the segregation bands accentuated by the manufacturing process. Together, they concisely describe the isotropy evolution.

The ESR process achieved a substantial global homogeneity boost by reducing all measures by around 50%. The vertical component was reduced to a greater extent than the horizontal one, improving the isotropy by 13% compared to the original cast & rolled material. The longer of the two annealing treatments accomplished a practically isotropic structure exhibiting a value of 0.979. It also decreased the mean variogram value by 25% and 36% in the horizontal and vertical directions, respectively. In contrast to the cast & rolled specimen, the five-hour annealing efficiently constrained the variance of the variograms, reducing the gap between minimum and maximum values considerably. However, due to the declining driving force towards equilibrium, annealing time brings diminishing returns. The Gini variograms have relatively low values in the order of 10^{-2}. As the mean $\Delta G^{\gamma\to\alpha'}$ value is practically identical in all four specimens, the relative differences between the Gini parameters and the standard first-order variograms are equivalent. The observed dissimilarities in the difference measure Diff. in the horizontal and vertical directions stem from the fact that the vertical direction has more homogenization potential, as a result of accentuated chemical segregations associated with the manufacturing process.

Armed with the newly acquired quantitative information, we can go back to the qualitative assessment at the beginning of this section. Even though not completely segregation-free, the ESR specimen turned out to consistently exhibit the highest austenite stability homogeneity across all studied processing routes. The segregation state before the deformation is low enough to produce band-like structures that do not compromise austenite stability. This behavior results in an improved response to HEE: Egels et al. showed that ESR effectively reduces hydrogen-induced crack nucleation and slows their growth [42]. In this context, the absence of segregation structures observed in the 15 h-annealed sample is a rather deceptive trait. While it performs better than the other cast specimens, its lack of spatial correlation is not a direct indicator of favorable spatial distribution. As a last remark within this application example, we would like to highlight that the measured Gini-based metrics have only deceptively low values. The 2×10^{-2} difference between the cast & rolled and the ESR samples can result in a drastic decline of strength and ductility [42].

Additional investigations in this line of research include the systematical study of the diffusion annealing efficiency and the spatial analysis of local the stacking fault energy. In the case of the former, for instance, the combination of first-order variograms, mechanical testing, and crack analysis through digital image analysis can provide fundamental information to achieve more economic and sustainable heat treatment processes. The stacking fault energy, on the other hand, depends on the chemical composition and is thus also prone to segregation-induced inhomogeneities.

4. Comparison with texture descriptors

As mentioned in the introduction, it could be argued that the proposed geostatistical approach is not strictly needed; after all, standard image processing and analysis methods are already capable of describing textures. However, as we will discuss in the following paragraphs, these techniques have distinct drawbacks that make the variogram approach much better suited for the task at hand. In particular, we will address the descriptors derived from GLCMs [47]. These are popular in microscopy and computational biology because they enable structure characterization based on analysis of grayscale images [48]. An $L\times L$ GLCM stores the number of times that pixel pairs with values z_i and z_j occur at a distance h, with $i,j=1,2,\ldots,L$, where L is the number of gray levels. To put it differently, for each offset h, we compute a bivariate histogram, which we use to derive the descriptors. We repeat this process for each offset.

In the following, we will employ GLCMs on the mappings presented in the previous section. Consequently, as the probability of encountering an element with a given value is exactly zero, we will rescale and discretize the real-valued property maps of $\Delta G^{\gamma\to\alpha'}$ to compute the GLCM and derived descriptors, effectively turning them into grayscale images. The selected descriptors are Contrast and Homogeneity. We capitalize these when we refer to the parameters to differentiate them from the nouns *contrast* and *homogeneity*. Their mathematical definition will not be covered here as this is out of the scope of this work. Instead, we refer the reader to Chapter 11 of the book *Digital Image Processing* by Gonzalez [47]. In a nutshell, the Contrast measures the squared intensity differences between pixels at a distance h. It is thus zero when the image has no intensity changes in the selected direction. The Homogeneity descriptor quantifies how close or far away the GCLM is from a diagonal matrix and is bounded between zero and unity. A Homogeneity of one indicates no intensity changes in the considered direction.

Fig. 9 displays the Contrast and Homogeneity parameters for the vertical and horizontal directions of the mappings presented in Fig. 5, employing GLCMs with $L=256$. It is not surprising that the Contrast bears a striking resemblance with the variograms of order one we presented in Fig. 8: Its definition is essentially equivalent to that of the variogram of order two. There are two caveats, though. Firstly, with the rescaling and derivation of the GLCM, we lost the capability of actually expressing the inhomogeneities in physical units. The upper bound of the Contrast parameter is solely linked to the size of the GLCM. Secondly, the computation of just two directions for all four mappings took approximately 14 s, whereas the fast variogram computation of all directions and distances, as mentioned above, took just 3 s, also employing the workstation mentioned above.

The advantage of the GLCM approach is that it enables the computation of other descriptors such as the Homogeneity in Fig. 9(c) and (d). These might provide further insights into the data. Ultimately, the construction of a GLCM as an intermediate step carries more information and offers a variety of interpretations. MATLAB® provides built-in algorithms to compute two further descriptors: Correlation and Energy [47]. The Homogeneity descriptor also looks like the variogram, only flipped in the vertical direction; recall that higher homogeneity values

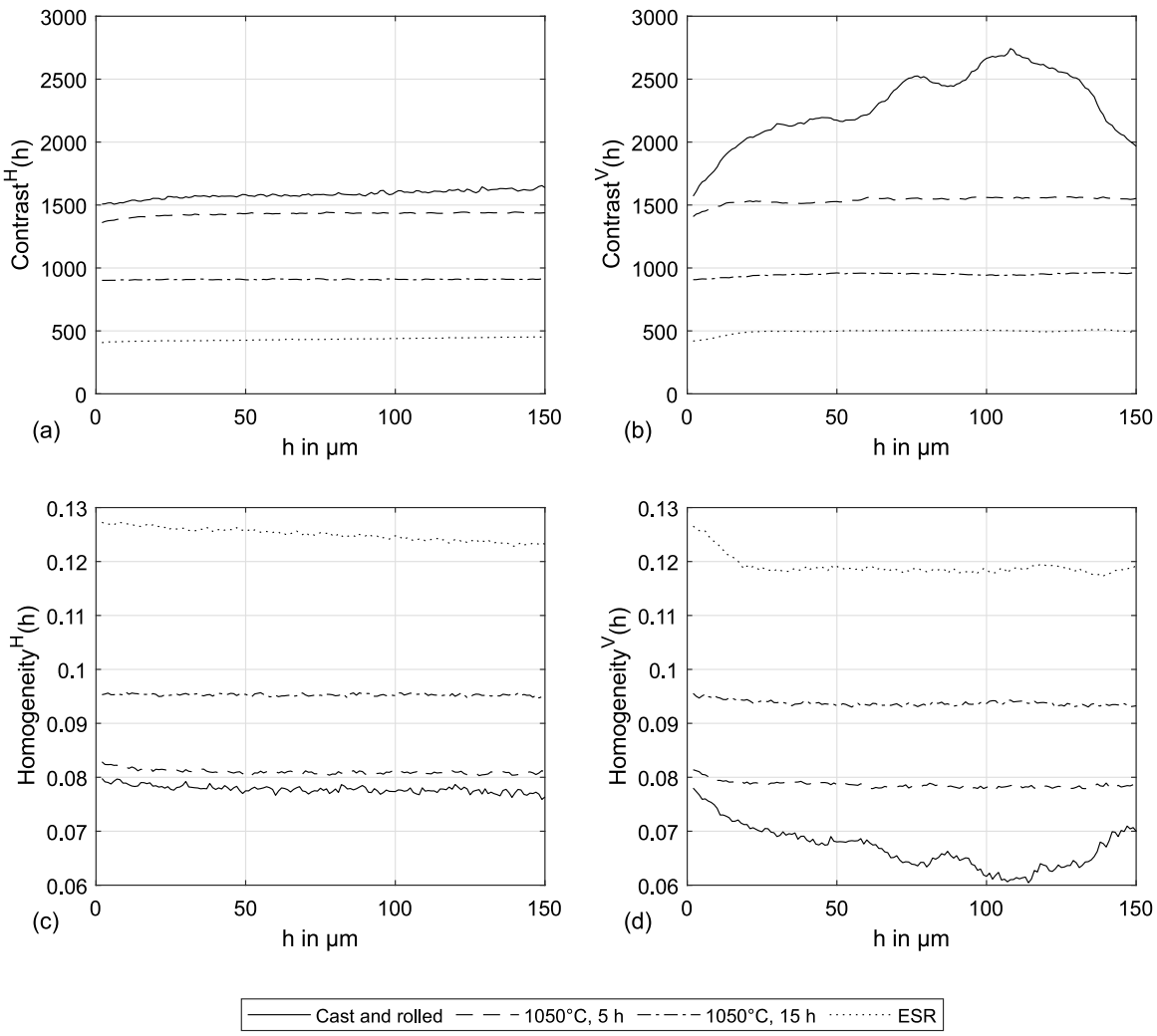

Fig. 9. Properties of the gray-level co-occurrence matrix. Computed Contrast (a) and (b) and Homogeneity (c) and (d) for the horizontal (a) and (c) and vertical (b) and (d) directions and all distances.

imply less randomness in the distribution of the intensity values. Essentially, this behavior arises because the Homogeneity concept is related to the definition of covariance. Two random variables whose bivariate histogram is predominantly limited to the main diagonal are strongly correlated. Oppositely, if the random variables are uncorrelated, the histogram will take a broader range of positive values elsewhere. The concepts of covariogram and correlogram are very similar in nature to the Homogeneity and Correlation of GLCMs [24,27] and can be also computed with fast algorithms [25,30].

In summary, the application of GLCMs to describe correlations in property maps has three fundamental drawbacks: (i) the real-valued matrices need to be converted to gray-level images, (ii) the resulting parameters lack immediate physical interpretation, and (iii) the computation times are several orders of magnitude larger. On the other hand, the grayscale texture analysis offers more flexibility and a broader palette of descriptors.

5. Summary and conclusions

In this work, we endeavored to showcase the advantages of using fast variograms of order one to quantitatively assess segregation-induced inhomogeneities in metallic materials. To that end, we examined the boundary conditions for their deployment in different segregation patterns and microstructures. Furthermore, we evaluated their efficiency and descriptive power in simulations and an empirical use case. Finally, we compared these algorithms with the GLCM texture descriptors of image processing and analysis, drawing parallels and conclusions along the way. All the scripts used were programmed in MATLAB®. Nevertheless, as they rely solely on standard functions, their development in other scientific programming languages is trivial.

We expect to see more applications of these techniques in materials science and engineering in the future, particularly in alloy and microstructural design. As briefly discussed at the beginning of Section 3, the application space of the presented method is twofold. On the one hand – and as shown in the application examples –, we can use this tool to characterize, rationalize, and predict micro and macroscopic properties. Further, the deployment of fast variograms in microstructural reconstruction tasks is especially promising. There, it can complement the already established two-point probability functions and physical descriptors [19,23,49] to create increasingly realistic and complex pseudo-random microstructures. These synthetic structures could then model segregations and segregation-induced property fluctuations in single and multiphase alloy systems [11]. Concretely, statistically quantifying metastable segregation states helps uncover new process-structure links specific to many technologically relevant materials. These include – drawing from the examples listed in the introduction – cobalt and nickel-base superalloys, high-entropy alloys, austenitic stainless steels, powder metallurgy tool steels, and metallic materials for the additive manufacturing processing route. Besides the case study of austenite stability we thoroughly handled in Section 3.2, we can mention a few technologically relevant examples:

- The efficiency evaluation and consequent optimization of the homogenization and solution treatments in superalloys. This can be achieved by studying the cost-benefit relationship based on spatial microsegregation, phase segregation and stability, and treatment cost.
- The geostatistical analysis of chemical inhomogeneities can shed light on the solidification process of metastable cellular microstructures. Correlation studies of the elemental mappings can determine the extent and range of contrary and co-segregation patterns in cells and cell walls.
- The systematical study of the composition gradient in high-entropy alloys can help develop new single-phase alloys. The precipitation of intermetallic phases can be circumvented by understanding the segregation tendencies and their arrangement in space.
- Selecting powder particle fractions according to their segregation structures could enable the fine-tuning of carbide size and shape distributions in HIP'ed high-alloy tool steels.

Ultimately, only through tailored segregation behavior, we can strive to improve the desired material properties. At the heart of this effort lies the presentation of a characterization method that is both statistical and has physical meaning. The juxtaposition is not often present in materials science and engineering, where, for example, n-point statistics are employed for microstructural reconstruction but rarely seen in technological applications. By showing the descriptive power of variograms of order one, their physical interpretation, and making the functions and algorithms directly available, we propose a common language for the characterization of segregation-driven inhomogeneities in metallic materials.

The reader can download the MATLAB® functions employed to generate this article, together with the raw data, from the supplementary materials section.

CRediT authorship contribution statement

Santiago Benito: Conceptualization, Methodology, Software, Visualization, Investigation, Formal analysis, Writing – original draft. **Gero Egels:** Resources, Data curation, Writing – original draft, Project administration. **Alexander Hartmaier:** Writing – review & editing, Supervision. **Sebastian Weber:** Writing – review & editing, Supervision, Funding acquisition.

Declaration of competing interest

The authors declare the following financial interests/personal relationships which may be considered as potential competing interests: Gero Egels reports financial support was provided by German Research Foundation. Sebastian Weber, Alexander Hartmaier reports financial support was provided by Ruhr University Bochum.

Data availability

Data will be made available on request.

Acknowledgments

We gratefully acknowledge the financial support from the Deutsche Forschungsgemeinschaft (DFG) within the project *'Entwicklung von Methoden zum Legierungsdesign für austenitische Stähle mit homogenem Verformungsverhalten und hoher Beständigkeit gegen Wasserstoffversprödung'* (DFG Project No.: WE 4436/7-1). We further acknowledge support through the Materials Science Postdoc Program at the Ruhr-University Bochum.

Santiago Benito would also like to thank Dr.-Ing Johannes Boes and Dr.-Ing Inmaculada Lopez-Galilea for the fruitful discussions.

Appendix A. Supplementary data

Supplementary material related to this article can be found online at https://doi.org/10.1016/j.mtcomm.2022.105016.

References

[1] J. Koßmann, C.H. Zenk, I. Lopez-Galilea, S. Neumeier, A. Kostka, S. Huth, W. Theisen, M. Göken, R. Drautz, T. Hammerschmidt, Microsegregation and precipitates of an as-cast Co-based superalloy—microstructural characterization and phase stability modelling, J. Mater. Sci. 50 (19) (2015) 6329–6338, http://dx.doi.org/10.1007/s10853-015-9177-8.

[2] L. Mujica Roncery, I. Lopez-Galilea, B. Ruttert, D. Bürger, P. Wollgramm, G. Eggeler, W. Theisen, On the effect of hot isostatic pressing on the creep life of a single crystal superalloys, Adv. Eng. Mater. 18 (8) (2016) 1381–1387, http://dx.doi.org/10.1002/adem.201600071.

[3] R. Fussik, G. Egels, W. Theisen, S. Weber, Investigation of the local austenite stability related to hydrogen environment embrittlement of austenitic stainless steels, Mater. Sci. Forum 941 (2018) 263–268, http://dx.doi.org/10.4028/www.scientific.net/MSF.941.263.

[4] J. Boes, A. Röttger, W. Theisen, Microstructure and properties of high-strength C + N austenitic stainless steel processed by laser powder bed fusion, Addit. Manuf. 32 (2020) 101081, http://dx.doi.org/10.1016/j.addma.2020.101081.

[5] J. Boes, A. Röttger, W. Theisen, Processing of X65MoCrWV3–2 cold work tool steel by laser powder bed fusion, Steel Res. Int. 91 (5) (2020) 1900445, http://dx.doi.org/10.1002/srin.201900445.

[6] A. Rodriguez-Lopez, B. Savoini, M. Monge, A. Muñoz, P. Pérez, Exploring CuCrFeVTi system to produce high entropy alloys for high heat flux applications, Nucl. Mater. Energy 29 (8) (2021) 101065, http://dx.doi.org/10.1016/j.nme.2021.101065.

[7] P. Suárez-Ocaño, S.G. Fries, I. Lopez-Galilea, R.D. Kamachali, J. Roik, L. Agudo-Jácome, The AlMo0.5NbTa0.5TiZr refractory high entropy superalloy: experimental findings and comparison with calculations using the CALPHAD method, Mater. Des. 217 (2022) 110593, http://dx.doi.org/10.1016/j.matdes.2022.110593.

[8] S. Benito, J. Boes, M. Matsuo, S. Weber, W. Theisen, Uncovering process-structure relationships associated to the hot isostatic pressing of the high-speed steel PMHS 3-3-4 through novel microstructural characterization methods, Mater. Des. 208 (12) (2021) 109925, http://dx.doi.org/10.1016/j.matdes.2021.109925.

[9] Q. Li, J. Xie, J. Yu, N. Sheng, D. Shu, G. Hou, J. Li, X. Sun, Y. Zhou, Effect of casting thickness on microstructure and mechanical properties of the high-W superalloy K416B, Mater. Today Commun. 29 (2021) 102916, http://dx.doi.org/10.1016/j.mtcomm.2021.102916.

[10] F. Sadeghi, T. Zargar, J.W. Kim, Y.-U. Heo, J.S. Lee, C.H. Yim, The effect of Ni depletion on athermal martensitic transformation in 304 austenitic stainless steel, Mater. Charact. 175 (2021) 111063, http://dx.doi.org/10.1016/j.matchar.2021.111063.

[11] Y. Pachaury, T. Kumagai, J.P. Wharry, A. El-Azab, A data science approach for analysis and reconstruction of spinodal-like composition fields in irradiated FeCrAl alloys, Acta Mater. 234 (2022) 118019, http://dx.doi.org/10.1016/j.actamat.2022.118019.

[12] M. Karunaratne, D.C. Cox, P. Carter, R.C. Reed, Modelling of the microsegregation in CMSX-4 superalloy and its homogenisation during heat treatment, in: T.M. Pollock, R.D. Kissinger, R. Bowman (Eds.), Superalloys 2000 (Ninth International Symposium), TMS, 2000, pp. 263–272, http://dx.doi.org/10.7449/2000/Superalloys_2000_263_272.

[13] K.G. Prashanth, J. Eckert, Formation of metastable cellular microstructures in selective laser melted alloys, J. Alloys Compd. 707 (1–2) (2017) 27–34, http://dx.doi.org/10.1016/j.jallcom.2016.12.209.

[14] R. Fussik, S. Weber, Local microstructural stability and hydrogen embrittlement of iron-base FCC alloys, J. Mater. Sci. Eng. A 6 (5) (2016) http://dx.doi.org/10.17265/2161-6213/2016.9-10.002.

[15] J. Man, I. Kuběna, M. Smaga, O. Man, A. Järvenpää, A. Weidner, Z. Chlup, J. Polák, Microstructural changes during deformation of AISI 300 grade austenitic stainless steels: Impact of chemical heterogeneity, Procedia Struct. Integr. 2 (2016) 2299–2306, http://dx.doi.org/10.1016/j.prostr.2016.06.288.

[16] F.R. Renzetti, L. Zortea, Use of a gray level co-occurrence matrix to characterize duplex stainless steel phases microstructure, Frat. Integr. Strut. 5 (16) (2011) 43–51, http://dx.doi.org/10.3221/IGF-ESIS.16.05.

[17] Y. Hu, Z. Wang, X. Fan, J. Li, A. Gao, Material microstructures analyzed by using gray level Co-occurrence matrices, Chin. Phys. B 26 (9) (2017) 098104, http://dx.doi.org/10.1088/1674-1056/26/9/098104.

[18] E.S. Thompson, P. Saveyn, M. Declercq, J. Meert, V. Guida, C.D. Eads, E.S.J. Robles, M.M. Britton, Characterisation of heterogeneity and spatial autocorrelation in phase separating mixtures using Moran's I, J. Colloid Interface Sci. 513 (2018) 180–187, http://dx.doi.org/10.1016/j.jcis.2017.10.115.

[19] R. Bostanabad, Y. Zhang, X. Li, T. Kearney, L.C. Brinson, D.W. Apley, W.K. Liu, W. Chen, Computational microstructure characterization and reconstruction: Review of the state-of-the-art techniques, Prog. Mater. Sci. 95 (4) (2018) 1–41, http://dx.doi.org/10.1016/j.pmatsci.2018.01.005.

[20] R. Hull, P. Keblinski, D. Lewis, A. Maniatty, V. Meunier, A.A. Oberai, C.R. Picu, J. Samuel, M.S. Shephard, M. Tomozawa, D. Vashishth, S. Zhang, Stochasticity in materials structure, properties, and processing-A review, Appl. Phys. Rev. 5 (1) (2018) http://dx.doi.org/10.1063/1.4998144.

[21] P. Kunjam, K. Shashidhar, S. Rakesh, D.R. Mahapatra, Stochastic modeling of the polygonal microstructures of alloys using representative microscopic images, Mater. Today Commun. 29 (2021) 102832, http://dx.doi.org/10.1016/j.mtcomm.2021.102832.

[22] P.-E. Chen, R. Raghavan, Y. Zheng, H. Li, K. Ankit, Y. Jiao, Quantifying microstructural evolution via time-dependent reduced-dimension metrics based on hierarchical n-point polytope functions, Phys. Rev. E 105 (2–2) (2022) 025306, http://dx.doi.org/10.1103/PhysRevE.105.025306.

[23] P. Seibert, A. Raßloff, K. Kalina, M. Ambati, M. Kästner, Microstructure characterization and reconstruction in python: MCRpy, Integr. Mater. Manuf. Innov. 11 (3) (2022) 450–466, http://dx.doi.org/10.1007/s40192-022-00273-4.

[24] J.-P. Chilès, Geostatistics: Modeling Spatial Uncertainty, second ed., in: Wiley Series in Probability and Statistics Ser, vol. 713, John Wiley & Sons Incorporated, Hoboken, 2012, URL https://ebookcentral.proquest.com/lib/kxp/detail.action?docID=693179.

[25] D. Marcotte, Fast variogram computation with FFT, Comput. Geosci. 22 (10) (1996) 1175–1186, http://dx.doi.org/10.1016/S0098-3004(96)00026-X.

[26] S. Torquato, Random Heterogeneous Materials: Microstructure and Macroscopic Properties, in: Interdisciplinary Applied Mathematics, vol. 16, Springer, New York, 2002, URL https://ebookcentral.proquest.com/lib/kxp/detail.action?docID=3085373.

[27] N.A.C. Cressie, Statistics for Spatial Data, revised ed., in: Wiley Classics Library, John Wiley & Sons Inc, New York and Chichester and Toronto and Brisbane and Singapore, 2015.

[28] A. Cecen, T. Fast, S.R. Kalidindi, Versatile algorithms for the computation of 2-point spatial correlations in quantifying material structure, Integr. Mater. Manuf. Innov. 5 (1) (2016) 1–15, http://dx.doi.org/10.1186/s40192-015-0044-x.

[29] D.T. Fullwood, S.R. Niezgoda, S.R. Kalidindi, Microstructure reconstructions from 2-point statistics using phase-recovery algorithms, Acta Mater. 56 (5) (2008) 942–948, http://dx.doi.org/10.1016/j.actamat.2007.10.044.

[30] K. Koch, J. Ohser, K. Schladitz, Spectral theory for random closed sets and estimating the covariance via frequency space, Adv. Appl. Probab. 35 (03) (2003) 603–613, http://dx.doi.org/10.1017/S0001867800012453.

[31] F. Loffredo, A. Scala, G.M. Adinolfi, F. Savino, M. Quarto, A new geostatistical tool for the analysis of the geographical variability of the indoor radon activity, Nukleonika 65 (2) (2020) 99–104, http://dx.doi.org/10.2478/nuka-2020-0015.

[32] P. Shi, W. Ren, T. Zheng, Z. Ren, X. Hou, J. Peng, P. Hu, Y. Gao, Y. Zhong, P.K. Liaw, Enhanced strength-ductility synergy in ultrafine-grained eutectic high-entropy alloys by inheriting microstructural lamellae, Nature Commun. 10 (1) (2019) 489, http://dx.doi.org/10.1038/s41467-019-08460-2.

[33] X.-S. Yang, Introduction to Computational Mathematics, World Scientific, 2015, http://dx.doi.org/10.1142/9404.

[34] C. San Marchi, T. Michler, K.A. Nibur, B.P. Somerday, On the physical differences between tensile testing of type 304 and 316 austenitic stainless steels with internal hydrogen and in external hydrogen, Int. J. Hydrogen Energy 35 (18) (2010) 9736–9745, http://dx.doi.org/10.1016/j.ijhydene.2010.06.018.

[35] T. Michler, A.A. Yukhimchuk, J. Naumann, Hydrogen environment embrittlement testing at low temperatures and high pressures, Corros. Sci. 50 (12) (2008) 3519–3526, http://dx.doi.org/10.1016/j.corsci.2008.09.025.

[36] L. Zhang, M. Wen, M. Imade, S. Fukuyama, K. Yokogawa, Effect of nickel equivalent on hydrogen gas embrittlement of austenitic stainless steels based on type 316 at low temperatures, Acta Mater. 56 (14) (2008) 3414–3421, http://dx.doi.org/10.1016/j.actamat.2008.03.022.

[37] G. Ghosh, G.B. Olson, Kinetics of f.c.c. → b.c.c. heterogeneous martensitic nucleation—I. The critical driving force for athermal nucleation, Acta Metall. Mater. 42 (10) (1994) 3361–3370, http://dx.doi.org/10.1016/0956-7151(94)90468-5.

[38] K. Mumtaz, S. Takahashi, J. Echigoya, L. Zhang, Y. Kamada, M. Sato, Temperature dependence of martensitic transformation in austenitic stainless steel, J. Mater. Sci. Lett. 22 (6) (2003) 423–427, http://dx.doi.org/10.1023/A:1022999309138.

[39] M. Martin, S. Weber, C. Izawa, S. Wagner, A. Pundt, W. Theisen, Influence of machining-induced martensite on hydrogen-assisted fracture of AISI type 304 austenitic stainless steel, Int. J. Hydrogen Energy 36 (17) (2011) 11195–11206, http://dx.doi.org/10.1016/j.ijhydene.2011.05.133.

[40] C. San Marchi, Hydrogen embrittlement of stainless steels and their welds, in: R. Gangloff, B. Somerday (Eds.), Gaseous Hydrogen Embrittlement of Materials in Energy Technologies, Woodhead Publishing, 2012.

[41] B.S. Kumar, V. Kain, M. Singh, B. Vishwanadh, Influence of hydrogen on mechanical properties and fracture of tempered 13 wt% Cr martensitic stainless steel, Mater. Sci. Eng. A 700 (3–6) (2017) 140–151, http://dx.doi.org/10.1016/j.msea.2017.05.086.

[42] G. Egels, L. Mujica Roncery, R. Fussik, W. Theisen, S. Weber, Impact of chemical inhomogeneities on local material properties and hydrogen environment embrittlement in AISI 304L steels, Int. J. Hydrogen Energy 43 (10) (2018) 5206–5216, http://dx.doi.org/10.1016/j.ijhydene.2018.01.062.

[43] T. Michler, Y. Lee, R.P. Gangloff, J. Naumann, Influence of macro segregation on hydrogen environment embrittlement of SUS 316L stainless steel, Int. J. Hydrogen Energy 34 (7) (2009) 3201–3209, http://dx.doi.org/10.1016/j.ijhydene.2009.02.015.

[44] R. Fussik, S. Weber, Derivation of property distribution images from microstructural analyses of X2CrNi18-9 with regard to hydrogen embrittlement, Pract. Metallogr. 55 (6) (2018) 387–399, http://dx.doi.org/10.3139/147.110522.

[45] K. Nohara, Y. Ono, N. Ohashi, Composition and grain size dependencies of strain-induced martensitic transformation in metastable austenitic stainless steels, Tetsu-To-Hagane 63 (5) (1977) 772–782, http://dx.doi.org/10.2355/tetsutohagane1955.63.5_772.

[46] S. Ahmadi, H. Arabi, A. Shokuhfar, A. Rezaei, Evaluation of the electroslag remelting process in medical grade of 316lc stainless steel, J. Mater. Sci. Technol. 25 (2009) 592–596.

[47] R.C. Gonzalez, R.E. Woods, Digital Image Processing, fourth ed., global ed., Pearson, New York, NY, 2018.

[48] D. Nikolovski, J. Cumic, I. Pantic, Application of gray level co-occurrence matrix algorithm for detection of discrete structural changes in cell nuclei after exposure to iron oxide nanoparticles and 6-hydroxydopamine, Microsc. Microanal. 25 (4) (2019) 982–988, http://dx.doi.org/10.1017/S1431927619014594.

[49] S. Benito, N. Wulbieter, F. Pöhl, W. Theisen, Microstructural analysis of powder metallurgy tool steels in the context of abrasive wear behavior: A new computerized approach to stereology, J. Mater. Eng. Perform. 28 (5) (2019) 2919–2936, http://dx.doi.org/10.1007/s11665-019-04036-9.